



High-resolution multimodal visible light optical coherence tomography and scanning laser ophthalmoscopy for *in vivo* neuronal and vascular retinal imaging in mice

SIYU SONG,^{1,2} GUANGRU BEN LIANG,^{1,2} TRISTAN T. HORMEL,¹
YUKUN GUO,^{1,2} MIN GAO,^{1,2} BENJAMIN SIVYER,¹ J. PETER
CAMPBELL,¹ SIYU CHEN,^{1,2} YIFAN JIAN,^{1,2} AND YALI JIA^{1,2,*}

¹Casey Eye Institute, Oregon Health & Science University, Portland, Oregon, USA

²Department of Biomedical Engineering, Oregon Health & Science University, Portland, Oregon, USA

*jiaya@ohsu.edu

Abstract: Microglial cells play a crucial role in retinal vascular and brain diseases through complex interactions with blood vessels and neurons. To image retinal structures, vasculature, and microglia, we developed a multimodal system integrating visible light optical coherence tomography (vis-OCT) and scanning laser ophthalmoscopy (SLO). Both subsystems achieve micron-scale resolutions and operate within the diffraction limit across a 34-degree field of view: theoretically, the OCT system offers an axial resolution of 2.12 μm and a transverse resolution of 8.78 μm, while the SLO system provides a transverse resolution of 7.1 μm. We validated the system performance using transgenic mice with fluorescent protein-labeled microglia, revealing detailed retinal microstructures, microvasculature, and individual microglia with distinguishable branches, confirmed by *ex vivo* microscopy.

© 2025 Optica Publishing Group under the terms of the [Optica Open Access Publishing Agreement](#)

1. Introduction

Microglia, the resident immune cells of the central nervous system, are distributed throughout the neural parenchyma of brain and retina [1]. Retinal microglia play an important role in tissue responses to injury and infection [2,3] and are engaged in retinal angiogenesis, including the branching, migration, and expansion of the vascular network [3,4]. Numerous studies have demonstrated microglia-related mechanisms in retinal degenerative and vascular diseases, such as age-related macular degeneration [5], hereditary retinopathies [6], glaucoma [7,8], retinopathy of prematurity [9], and diabetic retinopathy [10]. All of these references were demonstrated on rodent disease models. However, microglia can exacerbate tissue damage through neurotoxic and pro-inflammatory effects when overactivated [11]. Thus, imaging the dynamics of microglia is essential for understanding the retina and monitoring the response to various diseases that affect vision [12–14].

Dynamic imaging of retinal microglia can be categorized into *ex vivo* and *in vivo* approaches. In the former case, time-lapse confocal imaging has been widely reported [2,15]. Nevertheless, histological artifacts and removal of retinal tissue have the potential to strongly impact the native activity of microglia cells [16]. In comparison, *in vivo* imaging methods offer non-invasive access to neuron structures and biochemical processes in the retina. Among that, two-photon microscopy [17,18] has been used to monitor microglia behavior, but the field of view is limited (usually less than 500 μm). Scanning laser ophthalmoscopy (SLO) [14,16,19] has also been used. Although it can visualize individual microglia with great contrast, the axial resolution of SLO is low (usually worse than 100 μm) [12], making it hard to provide depth-resolved information.

And when the visualization of tissues and vasculature around microglia is needed, more SLO channels are needed [13].

Optical coherence tomography (OCT) is a non-invasive, three-dimensional, *in vivo* imaging modality with up to micron-scale axial and transverse resolutions. OCT angiography (OCTA), one of its functional extensions, provides an additional advantage of capturing blood flow, enabling the label-free detection of vascular structures down to the capillary. However, single cells are not very definitive in OCT, especially from the slabs with high reflectance signals, making it challenging to distinguish microglia clearly. In this case, OCT can be integrated with SLO to leverage the strengths of both modalities. While OCT and OCTA extract 3D retinal structures and vasculature, SLO can resolve microglia and contribute to a better understanding of OCT images. Several groups have developed multimodal OCT and SLO systems for this purpose [12,14,19–21], and most of these systems utilize near-infrared OCT (NIR-OCT) [12,14,19,21].

With these considerations, we proposed a multimodal visible light OCT (vis-OCT) and SLO system for *in vivo* retinal imaging. Compared to NIR-OCT, vis-OCT gains higher axial resolution with a comparable bandwidth [22] and allows for retinal oximetry [23–25]. Recent advancements in vis-OCT have achieved cellular-level structural imaging, successfully visualizing ganglion cell somas and photoreceptors [26]. In our design, vis-OCT and SLO share the same optical path, and both can achieve diffraction-limited performance across a 34-degree field of view (FOV), optimized via ray-tracing simulations in OpticStudio. The system performance was demonstrated with transgenic mice with fluorescent protein-labeled microglia. Moreover, we validated our results with *ex vivo* confocal microscopy.

2. Methods

2.1. System configuration

The schematic of the system is shown in Fig. 1. A supercontinuum laser (SuperK COMPACT, NKT Photonics Inc., Denmark) and a tunable filter (SuperK VARIA, NKT Photonics Inc., Denmark) provided a central wavelength of 580 nm with a bandwidth of ~100 nm illumination for the OCT subsystem. A 488 nm laser (0488L-15A, Integrated Optics, Lithuania) was used for the SLO subsystem and fluorescence excitation. Both light sources were connected to a 90/10 single-mode optical fiber coupler (FC1 in Fig. 1) for co-alignment, and the output light was divided into a sample and reference arm by another 75/25 fiber coupler (FC2 in Fig. 1). In the reference arm, a two-paddle manual fiber polarization controller (FPC020, Thorlabs Inc., USA) and a dispersion compensation block (LSM03DC-VIS, Thorlabs Inc., USA) were used to alter the polarization mismatch and dispersion mismatch between the two arms. In the sample arm, an electronically focus tunable lens (EI-10-30-CI-VIS, Optotune, Switzerland) was located before a 2D galvanometer-scanner (GVS002, Thorlabs Inc., USA) to alter the focal plane in the sample. The telescope (the inset figure in Fig. 1) consisted of two achromatic lenses with focal length of 125 mm (AC254-125-A, Thorlabs Inc., USA) that were placed symmetrically with a narrow air gap (smaller than 1 mm), another achromatic lens with a focal length of -75 mm (ACN254-075-A, Thorlabs Inc., USA), and a non-contact Slit Lamp Lens (90D, Volk Optical Inc., USA). The OCT back-scattered signal and SLO emission signal were separated by a customized dichroic mirror (zt510rb, Chroma Technology, USA) mounted at 45 degrees. Then, the OCT signal was directed to a commercial spectrometer (Cobra Vis, Wasatch Photonics, USA) with a line rate of 50 kHz, and OCT volumes were sampled at $2048 \times 300 \times 300$ points. The scanning pattern used in this study was raster scans, and three repeated B-scans at the same location were performed to generate OCTA signal. The theoretical axial and transverse OCT resolutions were 2.12 and 8.78 μm , respectively.

The SLO emission light was filtered by a single-band bandpass filter (FF03-510/20, Semrock, USA) and collected by a collimator connected to a multimode fiber (M43L01, Thorlabs Inc., USA), then directed to a photo-multiplier tube (H7827-002, Hamamatsu Photonics, Japan). The

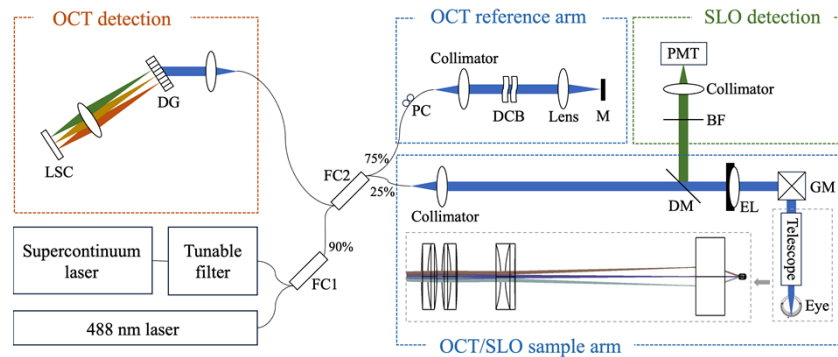


Fig. 1. Multimodal vis-OCT and SLO system schematic diagram. Light sources include a supercontinuum laser and a tunable filter for OCT, and a 488 nm laser for SLO. Both light sources are aligned by a fiber coupler (FC1) and enter the same sample arm after passing another fiber coupler (FC2). Back-scattered OCT signal and fluorescence emission signal are separated by a customized dichroic mirror (DM) and then collected by a spectrometer and a photomultiplier tube (PMT), respectively. Other optical components: PC: polarization controller; DCB: dispersion compensation block; M: mirror; BF: bandpass filter; EL: electronically focus tunable lens; GM: galvanometer-scanning mirrors; DG: diffraction grating; LSC: line scan camera. The telescope consists of four lenses, as shown in the inset.

SLO subsystem could operate alone at 1 MHz pixel rate with a sampling density of 500×500 points, and the theoretical transverse resolution was $7.1 \mu\text{m}$. As the SLO and OCT subsystems share the same scanning optics, they have the same FOV, greatly facilitating registration of the imaging data [12]. Hardware synchronization and data acquisition was controlled by custom software written in C/C++ language through a multifunction data acquisition card (PCIe-6351, National Instruments, USA). The incident power on the sample of OCT and SLO were 0.8 mW and 0.2 mW, respectively, adhering to the American National Standards Institute safety standards in ocular imaging.

2.2. Optical design and mechanical design

The sample arm optics were simulated with a mouse model eye [27] in OpticStudio (Ansys Inc., USA). The distances between the optical elements were optimized by minimizing the spot radius on the retinal plane and root mean square (RMS) wavefront error at all wavelengths. After passing through the telescope, the collimated beam with an initial diameter of 1.8 mm was reduced to 0.164 mm at the pupil. The spot diagrams on the retinal plane across a 34-degree FOV were demonstrated in Fig. 2(a). Since the optics were circular symmetric, only scanning angles oriented along the +x and +y directions were evaluated. In a practical optical system, the spot sizes within the Airy disk signify that the optical aberrations are low. According to the Rayleigh Criterion, high Strehl ratio values (above 0.8) imply that most of the light is focused effectively in a small region with no significant degradation in image quality [28]. The RMS wavefront error diagram further confirmed that the system could consistently operate within the diffraction limit for all wavelengths at all scanning angles (Fig. 2(b)). To test system performance like transverse resolution, a lens (C151TMD-A, Thorlabs Inc., USA) with a 2 mm focal length which is close to that of a mouse eye, was used.

To ensure precise alignment of optical components and precise locations of each component, SolidWorks (Dassault Systèmes, France) was used for the mechanical design (Fig. 3(a) and (b)). All the components were assembled with off-the-shelf products, with spacers and holders

designed according to the optical simulation and fabricated by a 3D printer with a resolution of 6.9 μm .

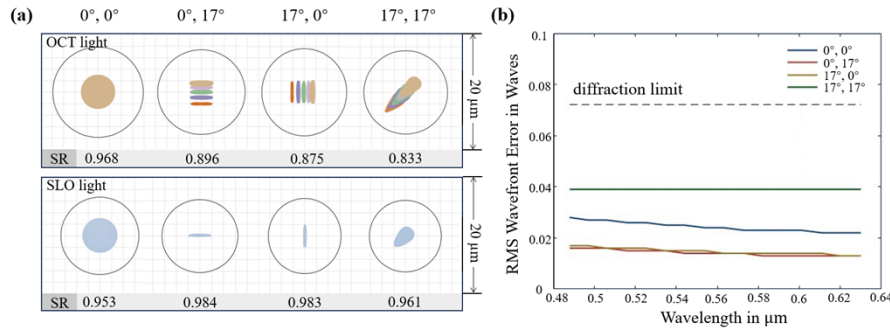


Fig. 2. Optical simulation in OpticStudio on the retinal plane. (a) Spot diagrams of OCT light (530, 550, 580, 605, 630 nm) and SLO light (488 nm) for different x- and y-direction FOV. Black circles represent the Airy disk with a 7.87 μm radius for OCT light and a 6.62 μm radius for SLO light. The Strehl ratios (SR) shown at the bottom row of each spot diagram are above 0.8 for all angles. Scale bars are 20 μm . (b) Root mean square (RMS) wavefront error in wavelengths, with four colors indicating various scanning angles. All RMS values are within the diffraction limit for all wavelengths across the whole FOV.

2.3. Animal handling

Transgenic mice (B6.129P2-Cx3cr1tm1Litt/J) with Enhanced Green Fluorescent Protein (EGFP)-labeled retinal microglia were purchased from the Jackson Laboratory and two male transgenic mice (8 weeks old) were used in this study. Prior to imaging, the mice were anesthetized with 5% isoflurane in a sealed box for 3 min, and the eyes were dilated with 1% tropicamide. Then, mice were immobilized on a customized imaging stage that was adjustable over five degrees of freedom and equipped with a customized head holder for inhalation gas delivery (2.5% isoflurane). During imaging, the body temperature was kept warm using a blanket circulated with 37°C water, as illustrated in Fig. 3(c). Another homemade holder was placed on the head to reduce motion artifacts caused by respiration. Artificial tears were used to prevent dehydration of the cornea.

2.4. Confocal microscopy imaging for validation

Microscopy imaging was conducted to validate the reliability of our system. Mice were euthanized by cervical dislocation after five days of *in vivo* imaging, and their eyes were drop-fixed in 4% paraformaldehyde for 30 minutes and washed for one hour in phosphate buffered saline (PBS). Retinas were stained with rabbit anti-GFP (1:2000) overnight at 40°C, washed for 1 hour in PBS, and then stained with Alexa-488 anti-rabbit (1:2000) and Lycopersicon Esculentum Lectin DyLight 649 (1:2000) for 2 hours at 40°C. Subsequently, the retinas were washed in PBS for 30 minutes and then cover slipped using a fluorogold mounting medium. The flat-mounted retinas were imaged two days later by a confocal microscope (TCS SP8, Leica Microsystems, Germany) and carried out at 118 depth positions. All the experimental procedures were approved by the Institutional Review Board/Ethics Committee and the Institutional Animal Care and Use Committee (IACUC) of Oregon Health & Science University (OHSU).

2.5. Image processing

Both OCT and SLO images were displayed in real time for fine adjustment using our custom GPU-accelerated software written in C/C++ [29,30]. Prior to the acquisition, eye alignment was performed using OCT system at low incident power (~ 0.5 mW) and sparse sampling density

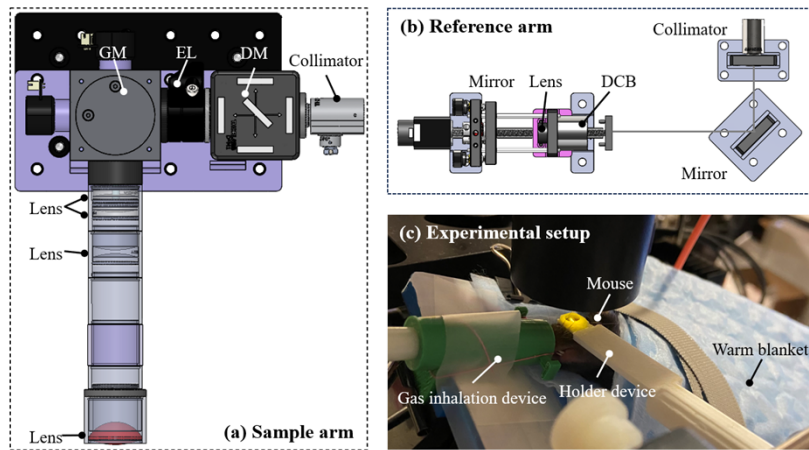


Fig. 3. (a) SolidWorks mechanical layout of the sample arm. GM: galvanometer-scanning mirrors; EL: electronically focus tunable lens; DM: dichroic mirror. (b) SolidWorks mechanical layout of the reference arm. DCB: dispersion compensation block. (c) Experimental setup illustrating how mouse eye was scanned. The head was immobilized on a customized gas inhalation device, with another customized holder device to minimize the motion caused by breathing. A warm blanket circulated with 37 °C water was used to maintain body temperature and comfort during imaging.

(100 × 100 points). Then, OCT and SLO data were captured successively using the protocols described above. OCT images were generated by standard post-processing steps in Matlab (MathWorks Inc., USA), similar to those published previously [31]. In brief, we removed the DC component of the interferometric fringe, resampled it to be linear in the k-domain, and digitally compensated for the remaining dispersion mismatch between the two arms. The structural information was retrieved by the fast Fourier Transform. For the images presented in this work, we used the following protocols: for OCT, one scan volume was recorded in 1.8 seconds; for OCTA, one scan volume was recorded in 5.4 seconds; and for SLO, 10 frames were recorded consecutively in 5 seconds. The OCT B-scan images were produced by averaging five adjacent B-scans within one volume. The SLO images were an average of 10 frames after registration using the StackReg function in ImageJ (National Institutes of Health, USA) [32].

Split-Spectrum Amplitude-Decorrelation Angiography algorithm [33] was used to generate OCTA signals, and a motion correction method was used to suppress bulk motion artifacts. A deep-learning algorithm was then performed to minimize the remaining noise [34,35]. After manually segmenting retinal layers using our lab-built software COOL-ART (Center for Ophthalmic Optics & Lasers-Angiography Reading Toolkit) [36,37], *en face* OCT was obtained using mean intensity projection, while *en face* OCTA was produced by maximum intensity projection.

3. Results

3.1. System characterization

The OCT system was characterized by measuring the transverse and axial resolutions, sensitivity, and intensity fall-off of the axial point spread function. A United States Air Force (USAF 1951) target was imaged, and it was possible to discern structures corresponding to group 6 and element 6, which are related to a line width of 4.38 μm and line spacing of 8.76 μm (Fig. 4(a)~(c)). This was close to the theoretical transverse resolution (8.78 μm). To assess system sensitivity, a protected silver mirror was placed at different depths in the sample arm, and 300 A-lines were averaged at each depth (Fig. 4(d)). Given that the light passed the neutral density filter (Thorlabs,

$OD = 3.0$) twice, the maximum sensitivity was 91 dB. The 6 dB fall-off depth was around 0.3 mm, which is enough to cover the whole mouse retina ($\sim 200 \mu\text{m}$). The axial resolution was around $2.2 \mu\text{m}$ in air, which was equivalent to $1.63 \mu\text{m}$ in tissue (refraction index of 1.35). This was measured as the -6 dB fall-off width of the intensity profile obtained from the mirror positioned at a depth of approximately $176 \mu\text{m}$ (Fig. 4(d)).

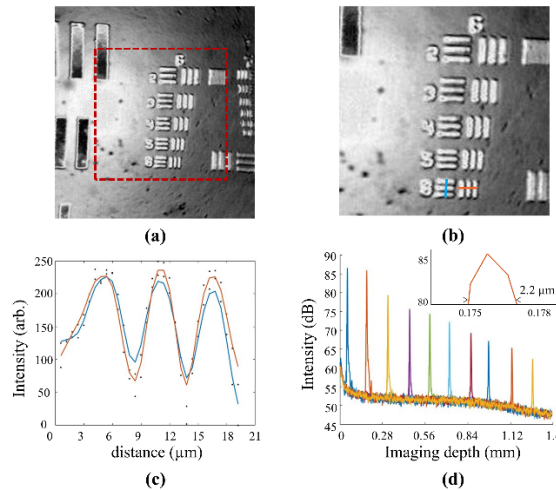


Fig. 4. (a) *En face* image of a standard USAF 1951 resolution test target imaged with vis-OCT. (b) A zoomed image of the red dashed box in (a), depicting the estimation of transverse resolution for group 6 and element 6 with $8.76 \mu\text{m}$ line spacing. (c) The fitted intensities for vertical and horizontal lines are marked in (b), showing that element 6 can be discerned. (d) Sensitivity fall-off across imaging depth of 1.4 mm, with different colors representing various depths. Maximum sensitivity is 91 dB, considering the light passes a neutral density filter ($OD = 3.0$) twice. Inset shows the measured axial resolution of $2.2 \mu\text{m}$ in air at a depth of $176 \mu\text{m}$.

3.2. Visible light OCT and OCTA imaging

En face OCT of the retina from Mouse 1 across 34-degree FOV demonstrated the network of major retinal blood vessels that radiated outward from the optic nerve head (Fig. 5(a)). Two cross-sectional images clearly delineated vessel boundaries and different retinal layers (Fig. 5(b) and (c)). In *en face* OCT of the nerve fiber layer (NFL), axon bundles were visualized (Fig. 5(d)), appearing as bright radial striations running from the retinal periphery toward the optic disk. Patterns of capillaries in the outer plexiform layer (OPL) (white stripes in Fig. 5(e)) and shadows from retinal capillaries, including inter-plexus capillaries (black dots in Fig. 5(f)) were observed.

To visualize the vascular map, OCTA was computed and generated. The *en face* OCT of the retina from Mouse 2 across a 24-degree FOV illustrated major blood vessels (Fig. 6(a)). The cross-sectional structural and angiographic image depicted multiple retinal layers and the location and relative intensity of the blood flow (Fig. 6(b)). *En face* OCTA was depth-colored, superimposed by nerve fiber layer (NFL), inner plexiform layer (IPL), and outer plexiform layer (OPL), as shown in Fig. 6(c).

3.3. SLO imaging of fluorescently labeled microglia

The SLO images in Fig. 7(a) and (b) were acquired when the focus was on the OPL, revealing the microglia distribution from Mouse 2 across a 24-degree FOV. They came from the same mouse eye, one week apart, and the scanning regions overlapped by 70%. Different types of microglia

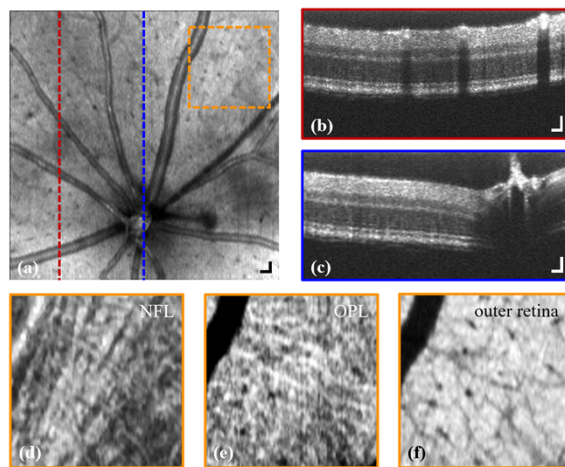


Fig. 5. OCT images of the retina from Mouse 1 across a 34-degree FOV. (a) *En face* OCT of the whole retina illustrating the major blood vessels (b, c) Cross-sectional OCT images located at two positions shown in (c). The vascular boundaries and retinal layers are distinctly resolved. (d-f) *En face* OCT of NFL (nerve fiber layer), OPL (outer plexiform layer), and the whole outer retina within the marked area in (c). The axon bundles (bright radial striations), patterns of capillaries (white stripes), and shadows from inter-plexus capillaries (black dots) are revealed, respectively. Scale bars: 50 μ m.

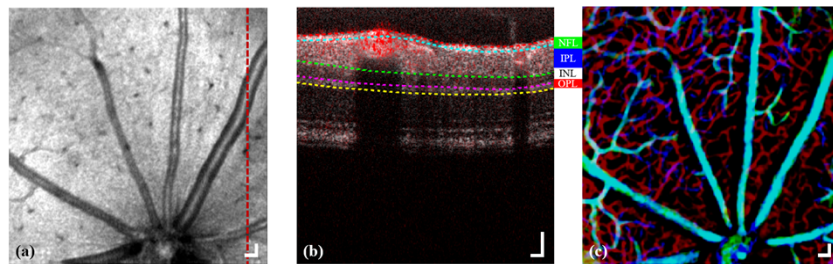


Fig. 6. OCT and OCTA images of the retina from Mouse 2 across a 24-degree FOV. (a) *En face* OCT with the optic disc at the edge. (b) Cross-sectional OCT image overlaid with the angiographic signal at the location shown in (a), with manually segmented inner retina layers. NFL: nerve fiber layer; IPL: inner plexiform layer; INL: inner nuclear layer; OPL: outer plexiform layer. (c) Overlaid *en face* OCTA of NFL (green), IPL (blue), and OPL (red), demonstrating organization of the retinal circulation. Scale bars: 50 μ m.

were observed, identified as homeostatic, rod, and amoeboid forms (Fig. 7(c)~(e)), which were highly consistent with the illustrations in the middle column (from BioRender) and right column (from confocal microscope), as well as other reports from SLO systems [13,14,19,38]. Within the overlapping scanning areas of Fig. 7(a) and (b), while the merged *en face* OCT (Fig. 7(g)) showed good alignment, there were distinct differences in microglia distribution (Fig. 7(f)). More amoeboid microglia were observed in the one-week capture (yellow circles in Fig. 7(f)).

3.4. Comparison of multimodal vis-OCT and SLO imaging with *ex vivo* microscopy imaging

To validate the reliabilities of our multimodal imaging system, *ex vivo* microscopy imaging was conducted on Mouse 2, one week later than the *in vivo* imaging. The cross-sectional and

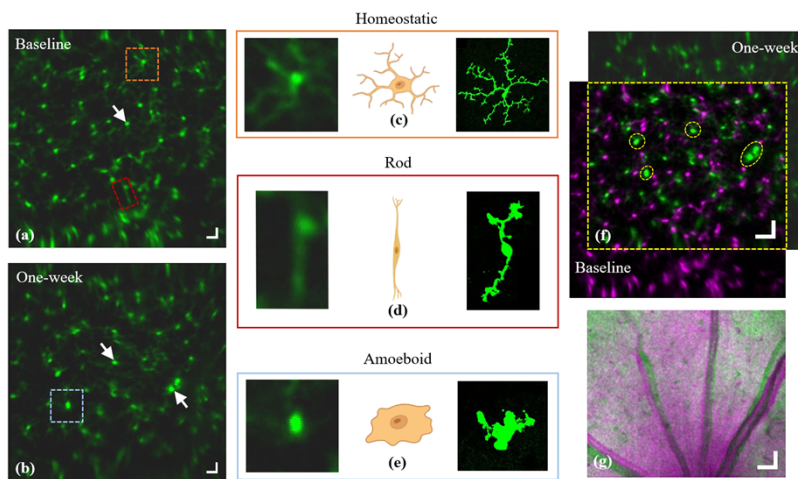


Fig. 7. (a) SLO image from Mouse 2 reveals the distribution of microglia across a 24-degree FOV. (b) SLO image of the same mouse eye captured one week later, with a 70% overlap of the scanning regions. Green bright dots (white arrows) in (a) and (b) represent microglia somas. (c-e) Enlarged areas highlighted in (a) and (b), showing homeostatic, rod, and amoeboid types of microglia, respectively. Illustrations in the middle column (from BioRender) and right column (from confocal microscope) show the corresponding microglia morphology. (f) Merged SLO image of microglia from the overlapping regions in (a) and (b), showing differences in microglia distribution. Yellow circles indicate amoeboid microglia. (g) The corresponding merged *en face* OCT of the overlapping regions, showing good alignment. Scale bars: 50 μm for (a) and (b), 100 μm for (g).

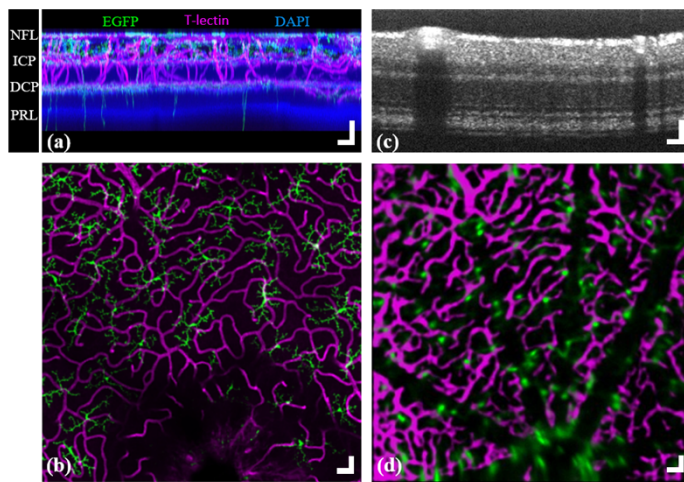


Fig. 8. (a) Cross-sectional microscopy image of the flat-mounted retina from Mouse 2 with microglia (EGFP; green), vasculature (T-lectin; magenta), and nuclei (DAPI; blue). The left labels indicate the retinal layers and vascular plexus with nerve fiber layer (NFL), intermediate capillary plexus (ICP), deep capillary plexus (DCP), and photoreceptor layer (PRL). (b) *En face* microscopy of the flat-mounted retina within OPL, showing the relative distributions of vasculature and microglia. (c) Cross-sectional OCT image of the living retina. (d) *en face* OCTA (magenta) of the living retina within OPL overlaid with the SLO image (green). Scale bars: 50 μm .

en face microscopy images of OPL clearly revealed the microglia distribution, as well as their surrounding vasculature and tissues (Fig. 8(a) and (b)). In comparison, although microglia could be hardly observed in the cross-sectional OCT image (Fig. 8(c)), the *en face* OCTA overlaid with the SLO image of OPL (Fig. 8(d)) showed the ability to indicate the relative locations of microglia and vasculature.

4. Discussion

We demonstrated a multimodal vis-OCT and SLO system for *in vivo* retinal imaging in mice. By integrating vis-OCT/OCTA and SLO modalities, this system provided a comprehensive platform for visualizing both the structural and vascular features of the retina while enabling detailed characterization of microglia distribution and morphology.

A key advantage of this system is that both OCT and SLO achieve high-resolution imaging. In comparison to the conventional NIR-OCT, vis-OCT can offer a higher axial resolution. The transverse resolutions for both are inversely proportional to the numerical aperture. In theory, a larger beam size on the pupil can provide a better transverse resolution. However, without an optimal optical design, simply increasing the beam size may result in larger optical aberrations and a lower transverse resolution [39]. This phenomenon is more pronounced with the visible light source. By optimizing the sample arm optics, we achieved low aberrations and maintained diffraction-limited performance across all wavelengths within a 34-degree FOV. Our results illustrated the capabilities of vis-OCT in achieving high-resolution imaging, allowing for precise segmentation of retinal layers and capillary-level detail visualization in OCTA images. And SLO provided single-cell resolution fluorescence imaging of EGFP-labeled microglia, capturing different microglia morphologies, including homeostatic, rod, and amoeboid types. Additionally, the shared scanning optics of OCT and SLO ensured a consistent FOV, greatly simplifying data registration between two modalities [12].

We also imaged the same mouse eye with one-week intervals to explore differences in microglia distribution. In the merged SLO image of the overlapping areas (Fig. 7(f)), discrepancies in microglia distribution were observed. The reason might be that the microglia had moved around, possibly triggered by some signs of abnormal cellular activity or the nature motility. This can be speculated by the increased presence of amoeboid microglia with larger somas in the latter capture, which represent activated microglia [40]. On top of that, the comparative results between the *in vivo* images and *ex vivo* microscopy images verified the reliability of our system, and the variance of microglia distribution further indicated their dynamic nature.

To fully leverage this vis-OCT and SLO imaging system and deepen understanding of microglia characteristics, several future explorations can be performed. First, as microglia play a pivotal role in neuronal damage or degeneration, this *in vivo* imaging system can be applied to mouse models with diseases. The assessment of microglia behavior in disease models can provide important information for learning pathological mechanisms [41]. Previous reports include models with laser-induced choroidal neovascularization [41], focal laser injury of blood vessel endothelial wall [42], and local damage to photoreceptors [14]. In addition, the system holds potential for investigating age-related retinal changes, including the gradual shifts in microglial morphology and distribution that occur during normal aging, thereby enabling longitudinal studies of neuroimmune remodeling in the healthy retina [43]. Second, assessing peripheral retinal conditions is important for some retinal vascular diseases, such as retinopathy of prematurity. The field of view of this system can be further expanded (up to 100 degrees), with a good transverse resolution (better than 10 μm), to cover the peripheral areas. Third, as vis-OCT enables retinal oximetry, the oxygen metabolism can be measured to provide more perspectives of retina conditions.

However, there are some limitations in our current work. Theoretically, OCT and SLO data can be acquired simultaneously, obtaining a wealth of complementary information in a single imaging

session. This feature was not utilized in this study because we used separate acquisition software, but an upcoming version of acquisition software will address this constraint. And although the optical simulation shows great performance, it is impossible to correct all the aberrations just by the optical design. The remaining aberrations can be solved by integrating aberration correction techniques. For instance, longitudinal chromatic aberrations can be corrected by adjusting the divergence of both OCT and SLO imaging beams to focus on the same depth [12]. And adaptive optics technology can be used to minimize the residual aberrations [13,19], although with a trade-off in the field of view. Last but not least, the transverse resolutions of OCT and SLO are not high enough since they are compromised to achieve a larger depth of focus (208 μm for OCT, covering almost the whole retina). Thus, it is difficult to resolve single microglia cells in the OCT images, and the branches of microglia in the SLO images are not very clear. To improve the transverse resolution, a more advanced optical design will be needed.

5. Conclusion

In this study, we presented a multimodal high-resolution system for *in vivo* mouse retinal imaging. The system captures structural and angiographic information by OCT and OCTA modalities, and detects fluorescent signals by SLO modality. Our system holds potential for longitudinal studies of microglia dynamics in retinal vascular diseases or optic nerve disorders.

Funding. National Institutes of Health (R01 EY036429, R01 EY035410, R01 EY024544, R01 EY027833, R01 EY031394, R43 EY036781, R01 EY031331, R01 EY032564, P30 EY010572, T32 EY023211, UL1TR002369); the Jennie P. Weeks Endowed Fund; the Malcolm M. Marquis, MD Endowed Fund for Innovation; Research to Prevent Blindness (Unrestricted Departmental Funding Grant, Dr. H. James and Carole Free Catalyst Award); Edward N. and Della L. Thome Memorial Foundation; Bright Focus Foundation (G2020168, M20230081).

Disclosures. Yali Jia: Visionix/Optovue (P, R), Roche/Genentech (P, R, F), Ifocus Imaging (I, P), Optos (P), Boehringer Ingelheim (C), Kugler (R). Tristan T. Hormel: Ifocus Imaging (I). Peter Campbell: Siloam Vision (P, F), Genentech (R). Yifan Jian: Siloam Vision (P, F). Yukun Guo: Visionix/Optovue (P), Genentech (R), Ifocus Imaging (P). The potential conflicts of interest have been reviewed and managed by OHSU. Other authors declare no conflicts of interest related to this article.

Data availability. Data underlying the results presented in this paper are not publicly available at this time but may be obtained from the authors upon reasonable request.

References

1. G. W. Kreutzberg, "Microglia: a sensor for pathological events in the CNS," *Trends Neurosci.* **19**(8), 312–318 (1996).
2. K. J. Liang, J. E. Lee, Y. D. Wang, *et al.*, "Regulation of Dynamic Behavior of Retinal Microglia by CX3CR1 Signaling," *Invest. Ophthalmol. Vis. Sci.* **50**(9), 4444–4451 (2009).
3. G. Rathnasamy, W. S. Foulds, E.-A. Ling, *et al.*, "Retinal microglia – A key player in healthy and diseased retina," *Prog. Neurobiol.* **173**, 18–40 (2019).
4. T. Arnold and C. Betsholtz, "Erratum to: The importance of microglia in the development of the vasculature in the central nervous system," *Vasc. Cell* **5**(1), 12 (2013).
5. M. Boyce, Y. Xin, O. Chowdhury, *et al.*, "Microglia–Neutrophil Interactions Drive Dry AMD-like Pathology in a Mouse Model," *Cells* **11**(22), 3535 (2022).
6. T. Blank, T. Goldmann, M. Koch, *et al.*, "Early Microglia Activation Precedes Photoreceptor Degeneration in a Mouse Model of CNGB1-Linked Retinitis Pigmentosa," *Front. Immunol.* **8**, 1930 (2018).
7. A. I. Ramírez, R. de Hoz, J. A. Fernández-Albarral, *et al.*, "Time course of bilateral microglial activation in a mouse model of laser-induced glaucoma," *Sci. Rep.* **10**(1), 4890 (2020).
8. J. A. Fernández-Albarral, J. J. Salazar, R. de Hoz, *et al.*, "Retinal Molecular Changes Are Associated with Neuroinflammation and Loss of RGCs in an Experimental Model of Glaucoma," *Int. J. Mol. Sci.* **22**(4), 2066 (2021).
9. J. Liu, J. K. W. Tsang, F. K. C. Fung, *et al.*, "Retinal microglia protect against vascular damage in a mouse model of retinopathy of prematurity," *Front. Pharmacol.* **13**, 945130 (2022).
10. H. Xie, C. Zhang, D. Liu, *et al.*, "Erythropoietin protects the inner blood–retinal barrier by inhibiting microglia phagocytosis via Src/Akt/cofilin signalling in experimental diabetic retinopathy," *Diabetologia* **64**(1), 211–225 (2021).
11. M. L. Block, L. Zecca, and J.-S. Hong, "Microglia-mediated neurotoxicity: uncovering the molecular mechanisms," *Nat. Rev. Neurosci.* **8**(1), 57–69 (2007).
12. P. Zhang, A. Zam, Y. Jian, *et al.*, "In vivo wide-field multispectral scanning laser ophthalmoscopy–optical coherence tomography mouse retinal imager: longitudinal imaging of ganglion cells, microglia, and Müller glia, and mapping of the mouse retinal and choroidal vasculature," *J. Biomed. Opt.* **20**(12), 126005 (2015).

13. D. J. Wahl, R. Ng, M. J. Ju, *et al.*, "Sensorless adaptive optics multimodal en-face small animal retinal imaging," *Biomed. Opt. Express* **10**(1), 252 (2019).
14. E. B. Miller, P. Zhang, K. Ching, *et al.*, "In vivo imaging reveals transient microglia recruitment and functional recovery of photoreceptor signaling after injury," *Proc. Natl. Acad. Sci.* **116**(33), 16603–16612 (2019).
15. J. E. Lee, K. J. Liang, R. N. Fariss, *et al.*, "Ex Vivo Dynamic Imaging of Retinal Microglia Using Time-Lapse Confocal Microscopy," *Invest. Ophthalmol. Vis. Sci.* **49**(9), 4169–4176 (2008).
16. A. Joseph, D. Power, and J. Schallek, "Imaging the dynamics of individual processes of microglia in the living retina in vivo," *Biomed. Opt. Express* **12**(10), 6157–6183 (2021).
17. A. Maeda, G. Palczewska, M. Golczak, *et al.*, "Two-photon microscopy reveals early rod photoreceptor cell damage in light-exposed mutant mice," *Proc. Natl. Acad. Sci.* **111**(14), E1428–E1437 (2014).
18. Z. Qin, S. He, C. Yang, *et al.*, "Adaptive optics two-photon microscopy enables near-diffraction-limited and functional retinal imaging in vivo," *Light: Sci. Appl.* **9**(1), 79 (2020).
19. R. J. Zawadzki, P. Zhang, A. Zam, *et al.*, "Adaptive-optics SLO imaging combined with widefield OCT and SLO enables precise 3D localization of fluorescent cells in the mouse retina," *Biomed. Opt. Express* **6**(6), 2191–2210 (2015).
20. M. J. Ju, C. Huang, D. J. Wahl, *et al.*, "Visible light sensorless adaptive optics for retinal structure and fluorescence imaging," *Opt. Lett.* **43**(20), 5162 (2018).
21. P. Zhang, E. B. Miller, S. K. Manna, *et al.*, "Temporal speckle-averaging of optical coherence tomography volumes for in-vivo cellular resolution neuronal and vascular retinal imaging," *Neurophotonics* **6**(04), 1 (2019).
22. P. Chauhan, A. M. Kho, and V. J. Srinivasan, "From Soma to Synapse: Imaging Age-Related Rod Photoreceptor Changes in the Mouse with Visible Light OCT," *Ophthalmol. Sci.* **3**(4), 100321 (2023).
23. J. Yi, Q. Wei, W. Liu, *et al.*, "Visible-light optical coherence tomography for retinal oximetry," *Opt. Lett.* **38**(11), 1796–1798 (2013).
24. S. Pi, A. Camino, X. Wei, *et al.*, "Rodent retinal circulation organization and oxygen metabolism revealed by visible-light optical coherence tomography," *Biomed. Opt. Express* **9**(11), 5851–5862 (2018).
25. S. Pi, T. T. Hormel, X. Wei, *et al.*, "Retinal capillary oximetry with visible light optical coherence tomography," *Proc. Natl. Acad. Sci.* **117**(21), 11658–11666 (2020).
26. S. Pi, T. T. Hormel, X. Wei, *et al.*, "Imaging retinal structures at cellular-level resolution by visible-light optical coherence tomography," *Opt. Lett.* **45**(7), 2107–2110 (2020).
27. G. Bawa, T. V. Tkatchenko, I. Avrutsky, *et al.*, "Variational analysis of the mouse and rat eye optical parameters," *Biomed. Opt. Express* **4**(11), 2585–2595 (2013).
28. S. Ni, R. Ng, D. Huang, *et al.*, "Non-mydiatic ultra-widefield diffraction-limited retinal imaging," *Opt. Lett.* **49**(14), 3902–3905 (2024).
29. Y. Jian, K. Wong, and M. V. Sarunic, "Graphics processing unit accelerated optical coherence tomography processing at megahertz axial scan rate and high resolution video rate volumetric rendering," *J. Biomed. Opt.* **18**(02), 1 (2013).
30. X. Wei, A. Camino, S. Pi, *et al.*, "Real-time cross-sectional and en face OCT angiography guiding high-quality scan acquisition," *Opt. Lett.* **44**(6), 1431–1434 (2019).
31. S. Pi, A. Camino, M. Zhang, *et al.*, "Angiographic and structural imaging using high axial resolution fiber-based visible-light OCT," *Biomed. Opt. Express* **8**(10), 4595–4608 (2017).
32. P. Thevenaz, U. E. Ruttmann, and M. Unser, "A pyramid approach to subpixel registration based on intensity," *IEEE Trans. Image Process.* **7**(1), 27–41 (1998).
33. Y. Jia, O. Tan, J. Tokayer, *et al.*, "Split-spectrum amplitude-decorrelation angiography with optical coherence tomography," *Opt. Express* **20**(4), 4710–4725 (2012).
34. M. Gao, Y. Guo, T. T. Hormel, *et al.*, "Reconstruction of high-resolution 6×6-mm OCT angiograms using deep learning," *Biomed. Opt. Express* **11**(7), 3585–3600 (2020).
35. M. Gao, T. T. Hormel, J. Wang, *et al.*, "An Open-Source Deep Learning Network for Reconstruction of High-Resolution OCT Angiograms of Retinal Intermediate and Deep Capillary Plexuses," *Transl. Vis. Sci. Technol.* **10**(13), 13 (2021).
36. Y. Guo, T. T. Hormel, S. Pi, *et al.*, "An end-to-end network for segmenting the vasculature of three retinal capillary plexuses from OCT angiographic volumes," *Biomed. Opt. Express* **12**(8), 4889–4900 (2021).
37. Y. Guo, A. Camino, M. Zhang, *et al.*, "Automated segmentation of retinal layer boundaries and capillary plexuses in wide-field optical coherence tomographic angiography," *Biomed. Opt. Express* **9**(9), 4429–4442 (2018).
38. D. J. Wahl, Y. Jian, S. Bonora, *et al.*, "Wavefront sensorless adaptive optics fluorescence biomicroscope for in vivo retinal imaging in mice," *Biomed. Opt. Express* **7**(1), 1 (2016).
39. S. Ni, T.-T. P. Nguyen, R. Ng, *et al.*, "105° field of view non-contact handheld swept-source optical coherence tomography," *Opt. Lett.* **46**(23), 5878–5881 (2021).
40. M. Chen and H. Xu, "Parainflammation, chronic inflammation, and age-related macular degeneration," *J. Leukoc. Biol.* **98**(5), 713–725 (2015).
41. S. Crespo-Garcia, N. Reichhart, C. Hernandez-Matas, *et al.*, "In vivo analysis of the time and spatial activation pattern of microglia in the retina following laser-induced choroidal neovascularization," *Exp. Eye Res.* **139**, 13–21 (2015).
42. C. Alt and C. P. Lin, "In vivo quantification of microglia dynamics with a scanning laser ophthalmoscope in a mouse model of focal laser injury," in F. Manns, P. G. Söderberg, and A. Ho, eds. (2012), p. 820907.
43. M. R. Damani, L. Zhao, A. M. Fontainhas, *et al.*, "Age-related alterations in the dynamic behavior of microglia," *Aging Cell* **10**(2), 263–276 (2011).